ACS APPLIED MATERIALS & INTERFACES

Research Article

www.acsami.org

# Cobalt Carbonate/ and Cobalt Oxide/Graphene Aerogel Composite Anodes for High Performance Li-Ion Batteries

Mohammad Akbari Garakani, Sara Abouali, Biao Zhang, Curtis Alton Takagi, Zheng-Long Xu, Jian-qiu Huang, Jiaqiang Huang, and Jang-Kyo Kim*

Department of Mechanical and Aerospace Engineering, The Hong Kong University of Science and Technology, Clear Water Bay, Kowloon, Hong Kong

Supporting Information

**ABSTRACT:** Nanocomposites consisting of ultrafine, cobalt carbonate nanoneedles and 3D porous graphene aerogel ($CoCO_3$/GA) are in situ synthesized based on a one-step hydrothermal route followed by freeze-drying. A further heat treatment produces cobalt oxide nanoparticles embedded in the conductive GA matrix ($Co_3O_4$/GA). Both the composite anodes deliver excellent specific capacities depending on current density employed: the $CoCO_3$/GA anode outperforms the $Co_3O_4$/GA anode at low current densities, and vice versa at current densities higher than 500 mA $g^{-1}$. Their electrochemical performances are considered among the best of similar composite anodes consisting of $CoCO_3$ or $Co_3O_4$ active particles embedded in a graphene substrate. The stable multistep electrochemical reactions of the carbonate compound with a unique nanoneedle structure contribute to the excellent cyclic stability of the $CoCO_3$/GA electrode, whereas the highly conductive networks along with low charge transfer resistance are responsible for the high rate performance of the $Co_3O_4$/GA electrode.

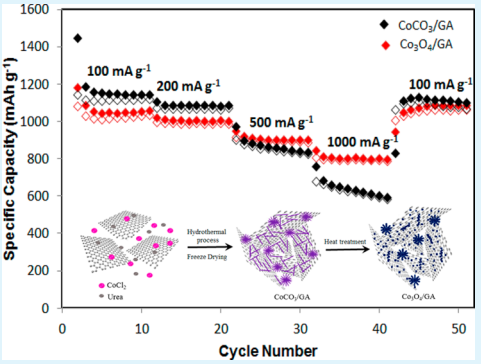


**KEYWORDS:** *graphene aerogel, cobalt carbonate, cobalt oxide, hydrothermal process, anode, Li-ion battery*

## 1. INTRODUCTION

Rechargeable lithium-ion batteries (LIBs) have been considered one of the most attractive energy storage devices due to their excellent electrochemical performance and large energy density compared to other electrochemical energy carriers.[1,2] Commercial LIBs use graphite as the anode material with a low theoretical specific capacity of 372 mAh $g^{-1}$, necessitating extensive research to develop substitute anode materials with higher energy/power densities for high performance LIBs to satisfy demanding applications like electric vehicles.[3] Various materials including nanostructured metal oxides, e.g., $SnO_x$,[4] $ZnO_x$,[5] $FeO_x$,[6] $MnO_x$,[7] $CoO_x$,[8−10] and metal oxysalts, e.g., carbonates, oxalates, oxyhydroxides and oxyfluorides, have been regarded as potential anode materials due to the advantages of high reversible capacities, high safety and long cyclic performance. In particular, cobalt oxides and cobalt oxysalts have attracted extensive attention because of their exceptional physical and electrochemical properties that can meet the demanding requirements of high performance LIBs.[11]

However, the large volume expansion/contraction and severe particle aggregation taking place in these metal compounds during the Li insertion/extraction processes often lead to electrode pulverization and loss of interparticle contacts, consequently resulting in large irreversible capacities and poor cyclic stability.[12,13] To address these issues, different strategies have been employed, including the use of carbon-based nanomaterials as the matrix to buffer the volumetric strains.[14−16] Graphene, a single layer of graphite with 2D arrays of $sp^2$ hybridized carbon atoms, has exceptional properties, such as excellent electrical conductivity, extremely large surface area, structural flexibility and chemical stability, which are useful attributes that can enhance the electrochemical performance of LIBs. An especially attractive option is to develop highly flexible binder-free electrodes consisting of graphene or graphene oxide (GO) sheets as the essential component. However, graphene or GO sheets tend to restack together due to van der Waals forces and hydrogen bonds between them when they are assembled using solution casting or vacuum filtration. The restacking may lead to severe agglomeration of graphene sheets, preventing Li-ion intercalation.[17−19]

In light of the above-mentioned restacking issue of 2D graphene sheets, 3D graphene structures have been considered an alternative solution for energy storage devices, owing to their unique network structure, large specific surface area, enhanced electron and ion transport, good mechanical integrity and outstanding electrical properties.[20,21] A self-assembled 3D graphene aerogel (GA) consisting of interconnected hierarchical porous networks has been synthesized via a one-step hydrothermal method.[22,23] Nanostructured active materials with inherently high capacities have also been incorporated

Received: July 23, 2014
Accepted: October 15, 2014
Published: October 15, 2014

  

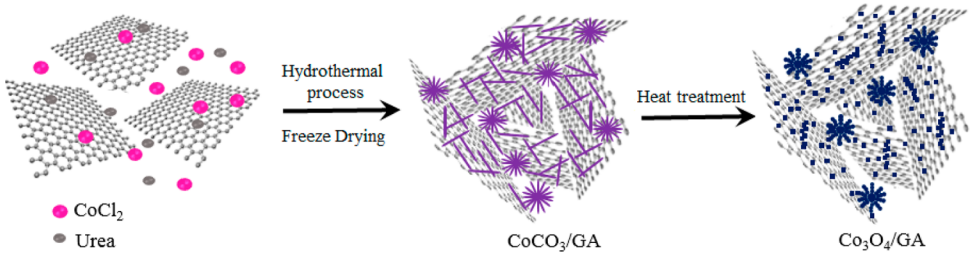


**Figure 1.** Schematic illustration of the synthesis process of $CoCO_3$/GA and $Co_3O_4$/GA composites.

into the 3D graphene aerogel through homogeneous dispersion of a metal precursor in GO dispersion followed by reduction.[24,25] These structures have shown enhanced electron and ion transport due to the short distance between the electrode and electrolyte, thus leading to improved rate performance and cyclic stability.

Following our recent studies on the application of 2D GO sheets for the synthesis of high performance electrodes,[26,27] we report a facile, hydrothermal method to synthesize cobalt-based nanoparticle/GA composites as anodes in LIBs. The reduction process of GO was optimized to synthesize the 3D GA substrate on which the high capacity nanoparticles, $CoCO_3$ and $Co_3O_4$ possessing an acicular structure, were in situ created. It is shown that the 3D porous, highly conducting graphene network, together with the active nanoneedles, delivered exceptionally high capacities, making the composites an ideal candidate for anodes in the next-generation LIBs.

## 2. EXPERIMENTAL SECTION

**2.1. Synthesis of $CoCO_3$/GA and $Co_3O_4$/GA Nanocomposites.** GO dispersion was prepared based on the modified Hummers method using natural graphite flakes that were thermally expanded at 1050 °C for 15 s after intercalation with $H_2SO_4$ to obtain expanded graphite (EG).[28,29] $H_2SO_4$ and $KMnO_4$ were mixed with EG and kept at 60 °C for 24 h. The mixture was transferred to an ice bath, deionized (DI) water and later, $H_2O_2$ was added. After the mixture was stirred for 30 min, the GO particles were washed with HCl solution and centrifuged for three times. DI water was used to wash the GO until the pH reached 5−6. The GO solution was further diluted with DI water to 2 mg $mL^{-1}$.

$CoCl_2{\cdot}6H_2O$ (1 mmol, Sigma-Aldrich) and urea (1 mmol, Sigma-Aldrich) were added to 60 mg of GO, and the mixture was stirred for 1 h. The mixture was transferred to a 45 mL Teflon-lined stainless steel autoclave and treated at 120 °C for 16 h as the optimized hydrothermal process condition that was chosen after extensive preliminary experiments to obtain GA with an acceptable degree of reduction, microstructural consistency and electrochemical performance. After the mixture cooled to room temperature, the graphene hydrogel containing $CoCO_3$ particles with light-pink deposits was washed with DI water. The mixture was stored at −20 °C for 24 h and then freeze-dried at −60 °C for 24 h in a freeze drier (Edwards Pirani 501 Super Modulyo freeze drier, Thermo Electron Corporation) to produce $CoCO_3$/GA. The $CoCO_3$/GA composite was heat-treated at 300 °C for 2 h in air to produce $Co_3O_4$/GA. Figure 1 schematically illustrates the process, including the hydrothermal treatment and freeze-drying, employed to synthesize the $CoCO_3$/GA and $Co_3O_4$/GA composites.

**2.2. Characterization.** The atomic structures of the $CoCO_3$/GA and $Co_3O_4$/GA composites were characterized by a powder X-ray diffraction (XRD) system (PW1830, Philips) with Cu K$\alpha$ radiation from 20° to 80°. X-ray photoelectron spectroscopy (XPS, surface analysis PHI5600, Physical Electronics) was employed to evaluate the elemental compositions, using Al K$\alpha$ line as the excitation source. Scanning electron microscopy (SEM, JEOL 6300) and field emission transmission electron microscopy (FETEM, JEOL 2010F) were used to examine the micro- and nanostructural features. The surface area was measured using the Brunauer−Emmett−Teller (BET) method on a Coulter SA 3100 surface area instrument. Quantitative structural analysis of the electrode materials was conducted on a RM3000 micro Raman system (Renishaw PLC) with argon laser excitation at 514 nm. Thermogravimetric analysis (TGA) was conducted (TGA/DTA 92 Setaram II testing system) in air over a temperature range of 50−800 °C at a heating rate of 10 °C $min^{-1}$. The electrical conductivities were determined using the pressed pallets of samples on a four-probe resistivity/Hall system (HL5500PC, Bio-Rad).

**2.3. Electrochemical Measurements.** The electrochemical tests were carried out using CR2032 coin cells. The test electrodes were prepared by mixing the active materials with conductive carbon black (super P) and polyvinylidene fluoride (PVDF) as the binder dissolved in *N*-methyl-2-pyrrolidone (NMP) in the weight ratio of 80:10:10. The slurry was coated onto copper foil, from which pellets of 12 mm in diameter were cut to use as electrodes and the mass loading of the active material was 1−1.5 mg. The cells were assembled in an Ar-filled glovebox with a Li foil as the counter electrode, $LiPF_6$ (1 M) in ethyl carbonate (EC)/dimethyl carbonate (DMC) (1:1 by volume) as the electrolyte and a microporous polyethylene film (Celgard 2400) as the separator. The coin cells were subjected to cyclic tests at different current densities between 0 and 3 V on a battery tester (LAND 2001 CT). The cyclic voltammetry (CV) tests were performed between 0 and 3 V with a scan rate of 0.1 mV $s^{-1}$, and electrochemical impedance spectroscopy (EIS) was carried out in the frequency range from 1 Hz to 100 kHz on an electrochemical workstation (CHI660).

## 3. RESULTS AND DISCUSSION

**3.1. Microstructure and Characterization.** The morphology of the pristine GA produced via the hydrothermal and freeze-drying process is shown in Figure 2. GA had a porous structure consisting of multilayer graphene walls of about 20−500 nm in thickness and macropores ranging a few to a few tens of micrometers in diameter.

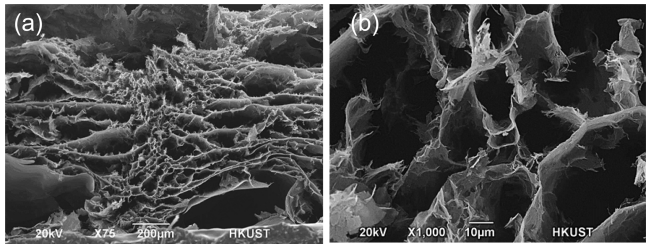


**Figure 2.** (a, b) SEM images of pristine graphene aerogel without cobalt compound taken at different magnifications.

The XRD pattern, SEM and TEM images of the $CoCO_3$/GA composites are shown in Figure 3. The XRD pattern (Figure 3a) indicates the presence of a mixture of cobalt carbonate (JCPDS no. 78-0209) with a sharp peak at $2\theta$ = 32.6° attributing to (104) reflection, and cobalt carbonate hydroxide hydrate (JCPDS no. 48-0083) at several diffraction angles. The

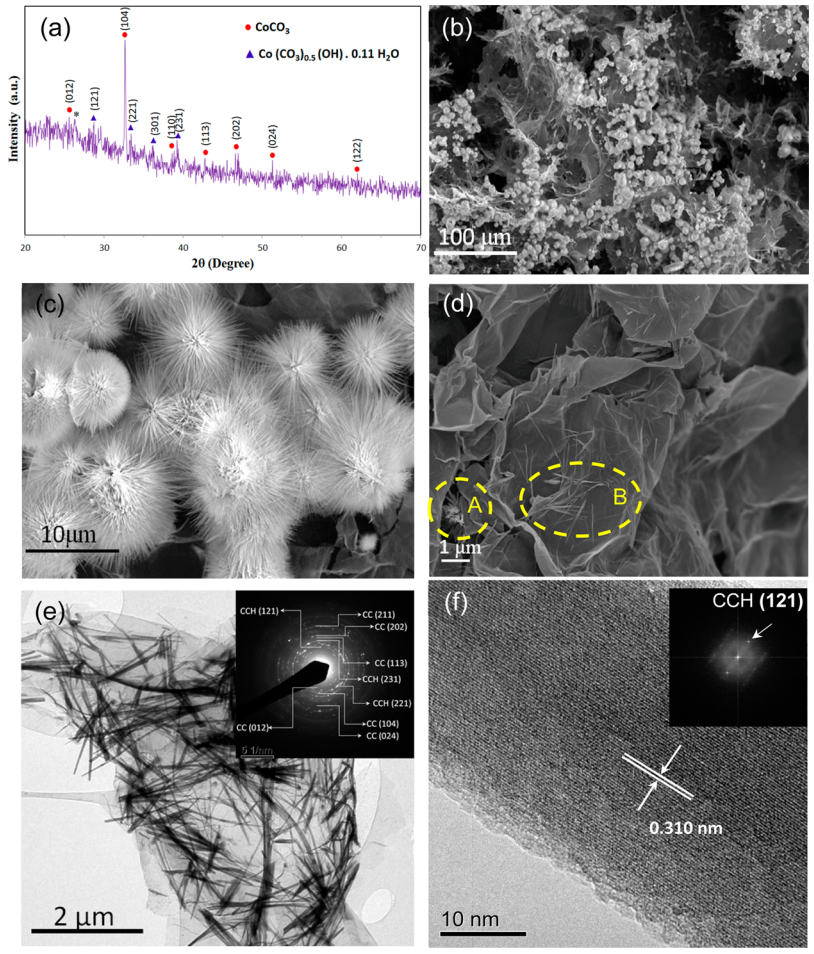


**Figure 3.** (a) XRD pattern (* indicating graphene peak), (b–d) SEM images (A, needles ball embedded between graphene layers; B, nanoneedles attached onto graphene), and (e, f) HRTEM images (with SAED and FFT patterns in the insets) of $CoCO_3$/GA composites (a mixture of cobalt carbonate (CC) and cobalt carbonate hydroxide hydrate (CCH)).

low-magnification SEM images (Figure 3b,c) present characteristic needle balls less than ∼10 μm in diameter that consisted of a myriad of acicular particles of ∼10–35 μm in diameter and 1–4 μm in length. These needles balls were embedded in the GA 3D structure. The SEM image (Figure 3d) and the HRTEM images (Figures 3e,f and S1, Supporting Information) show single-crystalline nanoneedles that were attached onto the graphene sheets. The selected area electron diffraction (SAED) pattern (inset of Figure 3e) presents the crystallographic structures of both cobalt carbonate (CC) and cobalt carbonate hydroxide hydrate (CCH). The rings can be attributed to the (211), (024), (202), (113), (104) and (012) reflections of CC with *d*-spacings of 0.151, 0.177, 0.194, 0.211, 0.274 and 0.355 nm, respectively; and the (231), (221) and (121) reflections of CCH with *d*-spacings of 0.227, 0.264 and 0.310 nm, respectively. The HRTEM image of a single-crystalline nanoneedle and the corresponding fast Furrier transform (FFT) pattern (Figure 3f) present CCH atomic planes with a *d*-spacing of 0.310 nm corresponding to the (121) reflection.

Figure S2 (Supporting Information) shows the SEM image of the cobalt carbonate-based compound processed at the same hydrothermal conditions without graphene. Needles obtained here were relatively thicker and more agglomerated than those formed in the presence of graphene. It appears that graphene effectively functioned as a support for metal oxides, preventing agglomeration and excessive growth of nanoparticles.[16]

The Raman spectra of GO, neat GA and $CoCO_3$/GA are shown in Figure S3 (Supporting Information). They indicate a marginal increase in intensity ratio, $I_D/I_G$, of the D band (located at 1341 $cm^{-1}$) to the G band (located at 1601 $cm^{-1}$) from 1.08 to 1.13 upon reduction of GO after the hydrothermal process, which is consistent with a previous report.[30] The ratio further increased to 1.18 in the $CoCO_3$/GA nanocomposite. The increase of $I_D/I_G$ is usually explained as a decrease in the average size but an increase in the number of $sp^2$ domains upon reduction.[31]

Cobalt carbonate, $CoCO_3$, is a member of calcite family with a rhombohedral structure where the C atoms occupy the triangular planar O-coordination, and the $CO_3^{2-}$ ions and Co occupy the octahedral spaces.[32,33] Cobalt carbonate-based compounds can be synthesized only under hydrothermal conditions according to the below reactions, which likely contain both physisorbed and chemisorbed water especially when they are formed in an aqueous solution. Here, the urea is the source of both carbonate and hydroxyl anions (eqs 1 and 2), while the cobalt cations come from cobalt chloride. Therefore, cobalt carbonate was produced according to eq 3, whereas cobalt carbonate hydroxide hydrate was produced according to eq 4.[32,34]

$$CO(NH_2)_2 + 3H_2O \rightarrow 2NH_4^+ + CO_2 + 2OH^- \quad (1)$$

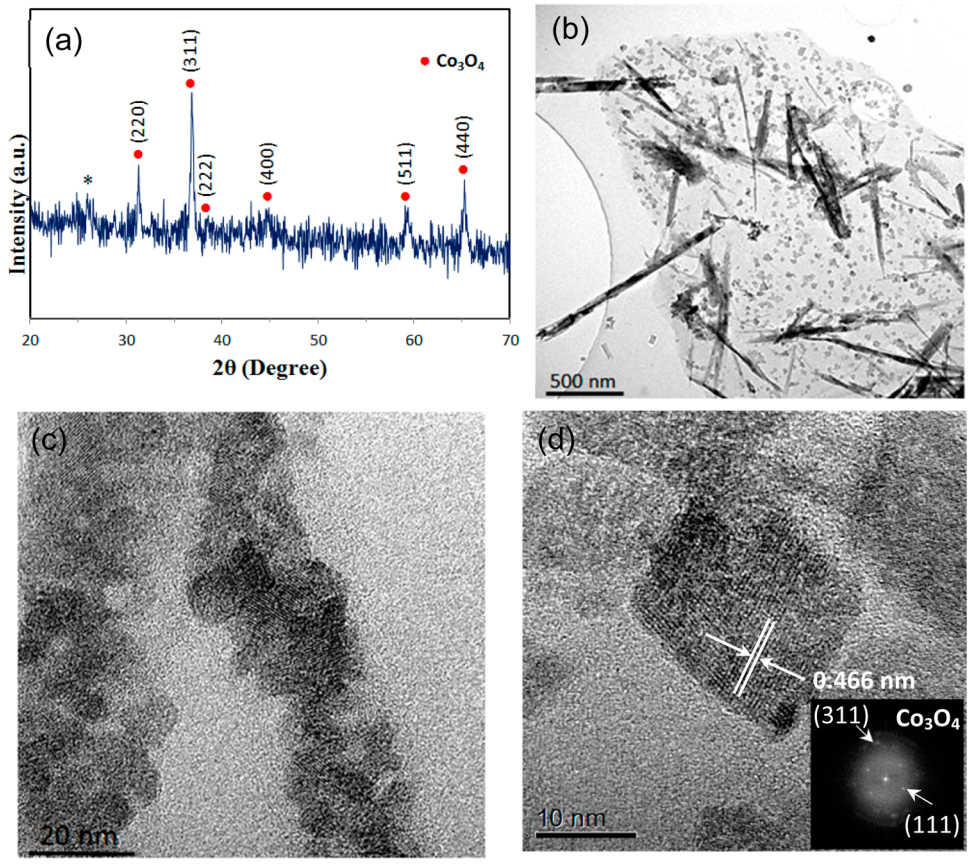


**Figure 4.** (a) XRD pattern (* indicating graphene peak), and (b–d) HRTEM images of $Co_3O_4$/GA composite with a FFT pattern in inset of panel d.

$$CO_2 + 2OH^- \rightarrow CO_3^{2-} + H_2O \quad (2)$$

$$Co^{2+} + CO_3^{2-} \rightarrow CoCO_3 \quad (3)$$

$$Co^{2+} + 0.5CO_3^{2-} + OH^- + 0.11H_2O \rightarrow Co(CO_3)_{0.5}(OH)\cdot 0.11H_2O \quad (4)$$

Several different methods have been employed to prepare nanostructured cobalt oxides with different morphologies. They include thermal decomposition and oxidation/reduction of cobalt-containing solid precursors, such as cobalt hydroxide, cobalt nitrate hydroxide, cobalt nitrate carbonate hydroxide, cobalt hydroxyoxide, and cobalt carbonate, under different atmospheric and thermal conditions.[34,35] In this work, the cobalt carbonate was decomposed to synthesize $Co_3O_4$ at a high temperature in air according to the following reaction:

$$3CoCO_3 + \frac{1}{2}O_2 \rightarrow Co_3O_4 + 3CO_2 \quad (5)$$

The TGA curve (Figure S4, Supporting Information) shows distinct regions of gradual weight loss: the initial weight loss of ~7.5% below ~180 °C was mainly due to the loss of adsorbed water. At temperatures up to ~300 °C, the intercalated water molecules evaporated and dehydroxylation took place. A further increase in temperature to about 520 °C resulted in simultaneous graphene burn-out and the transformation of carbonate phase to $Co_3O_4$, leading to a total weight loss of 68.8%. The graphene content was measured to be 57.7% from the weight loss of 11.4% due to the above phase transformation calculated using eq 5. The precursor completely transformed to $Co_3O_4$ at above 500 °C, causing almost no weight loss. Based on the TGA curve, the $Co_3O_4$ content in the nanocomposite was ~23.7 wt %. Assuming the original phase in neat $CoCO_3$ and eq 5, the $CoCO_3$ content in the nanocomposite was calculated to be 35.1 wt %.

Figure 4a presents the XRD pattern of heat-treated $Co_3O_4$ showing a significant diffraction peak at $2\theta$ = 36.84°, which is attributed to the (311) reflection (JCPDS no. 078-1970). The micro- and nanostructures of heat-treated $Co_3O_4$ particles are shown in SEM (Figure S5, Supporting Information) and HRTEM images (Figures 4b,c). After the heat treatment, needle balls and some nanoneedles attached on graphene still maintained their original shape as bundles while spherical or cubic nanoparticles of 5–20 nm in diameter were formed. This observation suggests that the transformation took place in two steps in which nanoneedles first broke into nanoparticles to form a linear structure consisting of interconnected particles (Figure 4c), followed by separation of nanoparticles in the next step (Figure 4d). According to the HRTEM and the inset FFT pattern (Figure 4d), the lattice structure belonged to $Co_3O_4$ with a *d*-spacing of 0.466 nm corresponding to the (111) reflection. Table S1 (Supporting Information) summarizes the BET surface areas and pore volumes of $CoCO_3$/GA and $Co_3O_4$/GA composites. To have a better comparison, the data for pure GA and neat $CoCO_3$ particles prepared in the same synthesizing conditions are also included. There were significant reductions in both specific surface area and pore volume by adding $CoCO_3$ nanoneedles or $Co_3O_4$ nanoparticles to the GA matrix. A similar observation has been reported previously in the $Fe_2O_3$/GA system.[36] The tendency of these

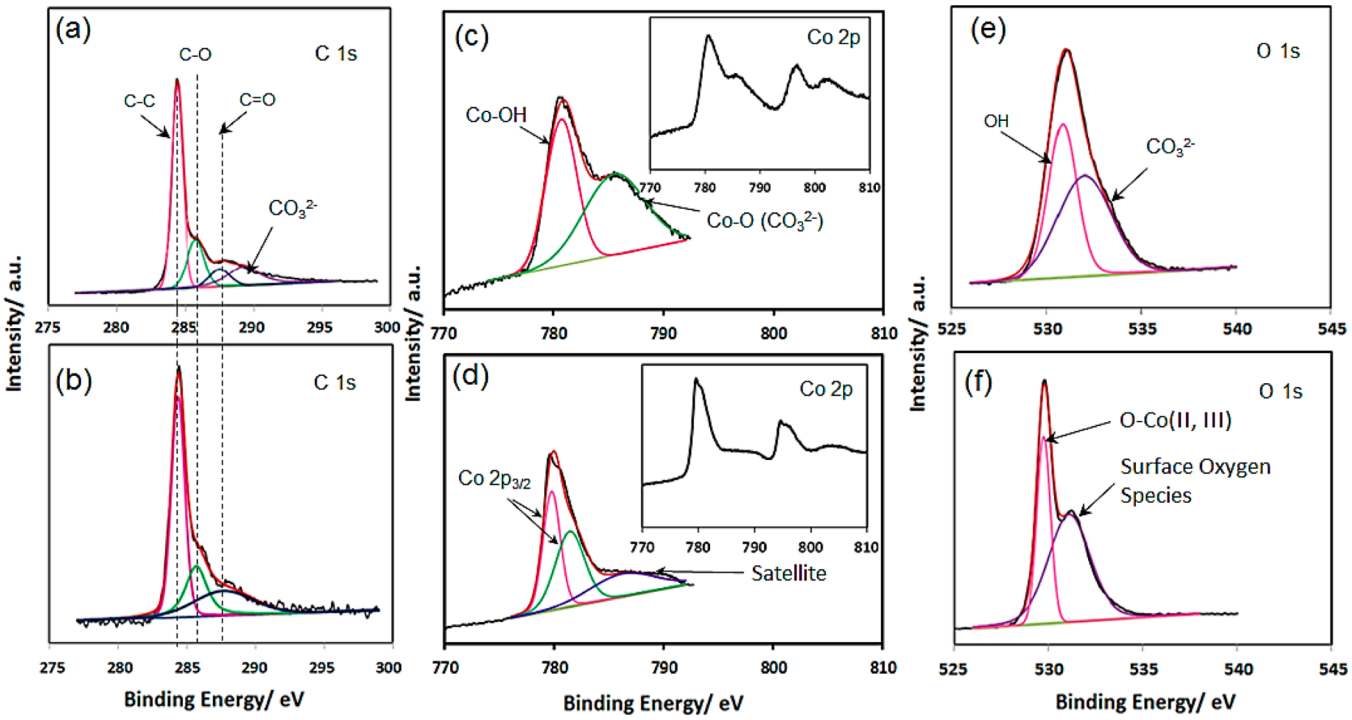


**Figure 5.** XPS deconvoluted (a, b) C 1s, (c, d) Co 2p and (e, f) O 1s spectra of $CoCO_3$/GA (a, c, e) and $Co_3O_4$/GA (b, d, f) composites. The insets in panels c and d are the Co 2p spectra in the wider range of binding energies.

nanoneedles and nanoparticles to agglomeration and blocking the GA pores may be responsible for the obtained surface area and pore volume.

The XPS results of the $CoCO_3$/GA and $Co_3O_4$/GA composites are displayed in Figure 5. The deconvoluted C 1s spectra had peaks at 284.4, 285.7, and 287.5 eV corresponding to the C—C, C—O and C═O bonds, respectively (Figures 5a,b). An additional peak was observed at 289.3 eV corresponding to the oxygen bonds in $CO_3^{2-}$ unit in $CoCO_3$/GA.[37−39] The Co 2p spectrum of $CoCO_3$/GA had three binding energies at 780.7 and 785.5 eV (Figure 5c). These binding energies can be assigned to the bonds of Co to OH units and Co−O bonds in cobalt carbonate units, respectively.[37] The binding energies of Co 2p peaks in $Co_3O_4$/GA (Figure 5d) were located at 779.8 and 781.4 eV, which are the characteristics of Co(II, III) to oxygen in $Co_3O_4$ and a satellite peak at 786.2 eV.[38,40] In the $CoCO_3$/GA composite (Figure 5e), two O 1s peaks were found at 530.8 and 531.9 that are attributed to the oxygen in hydroxide and carbonate groups, respectively.[37,39,41] In the $Co_3O_4$/GA composites (Figure 5f), a main peak was observed at 529.7 eV, which corresponds to the oxygen species in cobalt spinel oxide, whereas the shoulder at 531.1 eV is attributed to the surface oxygen defects or oxygen species in hydroxide groups adsorbed onto the surface.[39,42−44] These results are in a good agreement with eqs 1−3 presented above, as well as the XRD and SAED results (Figures 3 and 4).

**3.2. Electrochemical Properties.** The electrochemical performances of the $CoCO_3$/GA and $Co_3O_4$/GA electrode are shown in Figure 6. The cyclic performances of both the $CoCO_3$/GA and $Co_3O_4$/GA composite electrodes at a current density of 100 mA $g^{-1}$ were excellent with nearly 100% Coulombic efficiencies after 80 cycles (Figures 6a,d) whereas the corresponding performance by the neat GA and $CoCO_3$ electrodes were much lower. The above results indicate excellent electrochemical behavior and high cyclic stability of the $CoCO_3$/GA electrode compared to the control samples. This finding is attributed to the unique composite structure consisting of numerous $CoCO_3$-based nanoneedles that are embedded in the 3D GA architecture. The GA not only functioned as the substrate for the active material, but also formed the 3D conductive network and offered active sites for electrochemical reactions. The pore structure of 3D GA provided large spaces for the needle balls to grow into several micrometers in diameter during the hydrothermal synthesis process. Moreover, the incorporation of metal nanocompounds between the graphene sheets of GA naturally discouraged reagglomeration of graphene.

Several studies have recently been reported of high Li-storage capacities of metal carbonates, such as $MnCO_3$,[45] mixed carbonate $(Cd_{1/3}Co_{1/3}Zn_{1/3})CO_3$[32] and $CoCO_3$.[46] The stability of cobalt carbonate phase after cyclic tests was studied:[43,44] upon discharge, cobalt carbonate was converted to $Li_2CO_3$ and metallic Co, which were recovered back to the cobalt carbonate phase in the following charge process. Similar degradation in specific capacity was also reported because of poor electrical conductivity, volumetric change and particle aggregation during cycling. To overcome these problems, carbonaceous materials such as graphene nanosheets (GNS)[47] and polypyrrole (PPY)[48] have been introduced to the electrode material.

On the basis of the known Li storage mechanism of cobalt carbonate, it can be said that during the lithiation or discharge process, the active material transforms into metallic Co and $Li_2CO_3$, followed by partial reduction of $Li_2CO_3$ into carbon ($C^0$) or low-valence carbon ($C^{2+}$) and $Li_2O$. In the reverse delithiation or charge process, the Li-ions are extracted from carbon ($C^0$) or low-valence carbon ($C^{2+}$), followed by the participation of metallic Co in the oxidation reaction, resulting in the recovery of the original cobalt carbonate phase. These multistep reactions can be written as the following:[46,48]

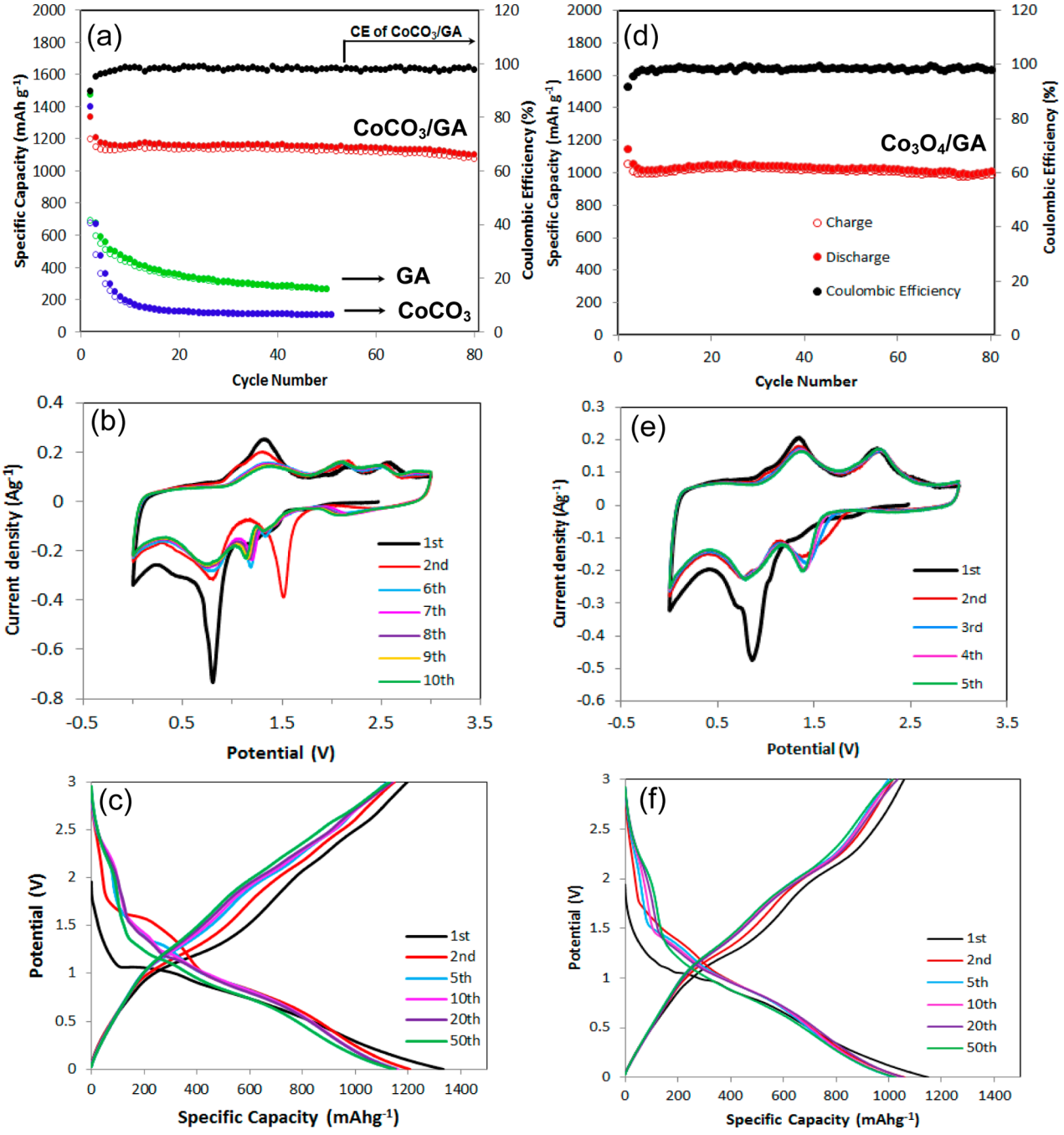


**Figure 6.** (a) Cyclic performance of the electrodes made from $CoCO_3$/GA, neat GA and cobalt carbonate-based particles at 100 mAh $g^{-1}$, (b) CV curves and (c) discharge/charge profiles of the $CoCO_3$/GA composite electrode, (d) cyclic performance at 100 mAh $g^{-1}$, (e) CV curves and (f) discharge/charge profiles of the $Co_3O_4$/GA electrode.

$$CoCO_3 + 2Li^+ + 2e^- \leftrightarrow Co + Li_2CO_3 \quad (6)$$

$$Co(CO_3)_{0.5}(OH) + 2Li^+ + 2e^- \leftrightarrow Co + 0.5Li_2CO_3 + LiOH \quad (7)$$

$$Li_2CO_3 + (4 + 0.5x)Li^+ + (4 + 0.5x)e^- \leftrightarrow 3Li_2O + 0.5(Li_xC_2) \quad (x = 0, 1, 2) \quad (8)$$

According to these reactions, if $C^{4+}$ ions in $Li_2CO_3$ are completely reduced to $C^0$, it follows then that the electrode would have up to 7 Li storage capacity, which is well fitted with the high capacity achieved in this study. To better understand the electrochemical behavior of $CoCO_3$/GA, cyclic voltammetry (CV) was performed at a scan rate of 0.1 mV $s^{-1}$ and the CV results along with the corresponding discharge/charge profiles are shown in Figures 6b,c, respectively. In the first cycle, $CoCO_3$/GA shows mainly two reduction peaks and three oxidation peaks. Among the reduction peaks, a minor broad peak appeared between 1.0 and 1.5 V that is attributed to the Li intercalation in the structure and reduction of cobalt carbonate hydroxide hydrate according to eq 7. The other major peak appeared between 0.4 and 1.0 V, including a sharp peak at 0.81 V with a shoulder at about 0.5 V, probably due to the reduction

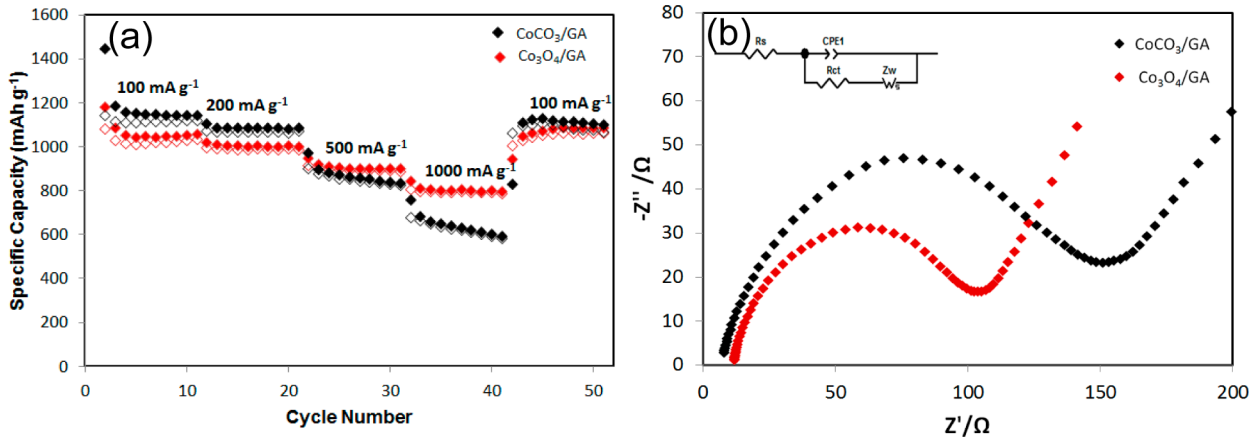


**Figure 7.** (a) Rate performances at different current densities and (b) Nyquist plots of $CoCO_3$/GA and $Co_3O_4$/GA electrodes over the frequency range of 100 kHz and 1 Hz.

of $CoCO_3$ to Co and $Li_2CO_3$ (i.e., conversion reaction), and the formation of solid electrolyte interface (SEI) layer followed by reduction of $C^{4+}$ to $C^0$/low valence C for the shoulder. In addition, three broad oxidation peaks at about 1.3, 2.16 and 2.56 V appeared that correspond to the oxidation of $C^0$/low valence C and formation of cobalt carbonate and cobalt carbonate hydroxide hydrate in the three successive steps.[46] In the second discharge process, the conversion peak was split into two peaks at 1.5 and 0.8 V resulting from the conversion reactions and reduction of high valence carbon to low valence, respectively. The upshift took place because SEI films were formed in the first discharge cycle while the electrode polarization occurred in the following cycles.[46−48] The conversion reaction peak was shifted gradually from 1.5 to 1.1 V during the six charge/discharge cycles. In the following cycles, the peak position was stable at 1.1 V, indicating excellent cyclic stability and reversibility of the active material. The above observations are also in a good agreement with the discharge/charge profiles at different cycles shown in Figure 6c.

The cyclic performance of the $Co_3O_4$/GA electrode (Figure 6d) was slightly lower than the $CoCO_3$/GA electrode (Figure 6a). It is found that the $Co_3O_4$ electrode obtained after heat treatment had a slightly lower Li-ion storage capacity than the as-prepared $CoCO_3$ electrode. During the discharge cycle, $Co_3O_4$ is converted to Co, which provides up to 8 Li storage for $Co_3O_4$ according to the following equation:[34]

$$Co_3O_4 + 8Li^+ + 8e^- \leftrightarrow 3Co^0 + 4Li_2O \quad (9)$$

The high capacity of $Co_3O_4$/GA after several cycles and the excellent rate performance can be attributed to the primary carbonate-based nanoneedles and particles that were formed in the porous 3D GA structure with extensive electrical networks. The high Coulombic efficiency during the charge/discharge cycles of the electrode may also be explained by the porous structure of GA with ample active sites for efficient and fast Li-ion transfer.[49]

It is also worth noting that both electrodes show significantly high initial Coulombic efficiencies at a low current density of 0.1 A $g^{-1}$, which can be attributed to the formation of SEI layer during the first discharge process and its high degree of decomposition during the subsequent charge process, leading to an extra capacity. It was previously shown that the decomposition of SEI depended on the catalytic activity of metallic nanoparticles.[50] In our study, metallic cobalt and $Li_2O$ were formed at the end of discharge process according to eqs 6−9. The nanoscale metallic cobalt acted as a catalyst, promoting the decomposition of SEI and $Li_2O$, giving rise to high Coulombic efficiencies.[49]

The CV curves of $Co_3O_4$/GA obtained at a scan rate of 0.1 mV $s^{-1}$ show one reduction and two oxidation peaks in the first cycle (Figure 6e). The sharp reduction peak located at 0.87 V and a small shoulder at 0.72 V correspond to the formation of SEI films and the reduction of $Co_3O_4$ to Co according to eq 9, respectively. During the first charge process, these two reactions took place in reverse directions at 1.32 and 2.14 V, respectively, indicating reversible charge/discharge behavior of $Co_3O_4$. In the following cycles, the major peak was split into two broad peaks at 0.6−1.1 V and 1.1−1.7 V as a result of the conversion reactions taking place at shifted positions in comparison with the first discharge cycle. These results are also in agreement with the charge−discharge profiles shown in Figure 6f.

The cyclic performance of both electrodes in the first 200 cycles at a high current density of 1 A $g^{-1}$ is shown in Figure S6 (Supporting Information), confirming their excellent stability. The $Co_3O_4$/GA and the $CoCO_3$/GA electrodes presented specific capacities of 832 and 660 mAh $g^{-1}$, respectively, after 200 cycles. The rate performances of both electrodes are shown in Figure 7a. When the current density was increased to 0.2, 0.5 and 1.0 A $g^{-1}$, the specific capacities of the $CoCO_3$/GA electrode gradually reduced to 1084, 835 and 594 mAh $g^{-1}$, respectively. The corresponding specific capacities of the $Co_3O_4$/GA electrode were 1001, 900 and 798 mAh $g^{-1}$, respectively, with a remarkable capacity retention of 75.5% when tested at 1.0 A $g^{-1}$. The comparison reveals an interesting observation that the latter electrode outperformed the former at low current densities up to 0.2 A $g^{-1}$ and the reverse was true at high current densities at or above 0.5 A $g^{-1}$. The high rate capacities of the $Co_3O_4$/GA electrode measured at current densities up to 4 A $g^{-1}$ are given in Figure S7 (Supporting Information). The specific capacities corresponding to 2 and 4 A $g^{-1}$ reached notable values of 645 and 513 mAh $g^{-1}$, respectively. The electrochemical impedance spectroscopy (EIS) was used to study the electronic conductivity and ion transfer behavior of the electrodes which supported the above finding. Figure 7b shows the Nyquist plots and the corresponding impedance parameters calculated using the Zview software are summarized in Table 1 along with the measured electrical conductivities. The equivalent series

**Table 1. Impedance Parameters Calculated from the Equivalent Circuit and the Corresponding Electrical Conductivities**

| electrode | $R_s$ (Ω) | $R_{ct}$ (Ω) | electrical conductivity (S cm$^{-1}$) |
|---|---|---|---|
| GA | | | $2.53 \times 10^{-2}$ |
| $CoCO_3$/GA | 6.5 | 146.9 | $5.09 \times 10^{-4}$ |
| $Co_3O_4$/GA | 10.9 | 97.5 | $5.9 \times 10^{-3}$ |

resistance, $R_s$, was lower for $Co_3O_4$/GA than for $CoCO_3$/GA, and vice versa for the charge transfer resistance, $R_{ct}$, in agreement with the electrical conductivity values. It is thought that the faster charge transfer of the $Co_3O_4$/GA electrode arose from the enhanced contact between the electrode and the electrolyte as well as better electrical connection between the particles and GA,[49] giving rise to the better high rate performance than the $CoCO_3$/GA electrode.

Finally, the capacities presented in this work are compared with those taken from the literature for various electrodes made from Co-based nanoparticles and graphene substrates, as shown in Table 2.[35,47,49−55] It is clearly seen that the results obtained from this study are considered among the highest and the most stable capacities reported so far for the anodes containing similar $CoCO_3$ or $Co_3O_4$ nanoparticles.

**Table 2. Comparison of Capacities between Similar Electrodes Reported Recently**

| materials | capacity (mAh g$^{-1}$) | current density (mA g$^{-1}$) | cycle number | ref |
|---|---|---|---|---|
| $CoCO_3$/graphene | 930 | 50 | 40 | 47 |
| $CoCO_3$/GA | 1102 | 100 | 80 | current study |
| $Co_3O_4$/graphene | 935 | 50 | 30 | 51 |
| $Co_3O_4$/graphene | ∼1000 | 50 | 50 | 49 |
| $Co_3O_4$/graphene | 673 | 180 | 100 | 35 |
| $Co_3O_4$/graphene | ∼840 | 100 | 40 | 52 |
| $Co_3O_4$/graphene | 778 | 200 | 42 | 53 |
| $Co_3O_4$/graphene | 900 | 100 | 60 | 54 |
| $Co_3O_4$/CoO/graphene | 779 | 50 | 50 | 55 |
| $Co_3O_4$/graphene | 1065 | 89 | 30 | 56 |
| $Co_3O_4$/GA | 1012 | 100 | 80 | current study |

## 4. CONCLUSION

We employed a simple hydrothermal process and freeze-drying to in situ synthesize cobalt carbonate-based nanoneedles that are embedded in the 3D porous structure of GA. Both as-prepared $CoCO_3$/GA and $Co_3O_4$/GA obtained after heat treatment were used as the anodes for LIBs, revealing exceptional cyclic performance and high rate capacities. The synergy arising from the 3D porous and conductive graphene substrate that offered plenty of active sites for efficient and fast Li-ion transfer, as well as the well-dispersed, ultrafine $CoCO_3$ nanoneedles and the $Co_3O_4$ nanoparticles, is responsible for the ameliorating results. The $CoCO_3$/GA electrode outperformed the $Co_3O_4$/GA electrode at low current densities, whereas the latter electrode exhibited a particularly superior high rate performance compared to the former electrode. These findings have practical implications in that the compositions of the electrodes can be tailored to suit end applications with different current density requirements.

## ASSOCIATED CONTENT

### Supporting Information

TEM image of $CoCO_3$/GA, SEM image of $CoCO_3$, Raman spectra of GO, neat GA and $CoCO_3$/GA, TGA curve of the $CoCO_3$/GA, SEM images of $Co_3O_4$/GA, cyclic performance of both electrodes at the current density of 1 A g$^{-1}$, rate performance of $Co_3O_4$/GA at high current densities and BET results. This material is available free of charge via the Internet at http://pubs.acs.org.

## AUTHOR INFORMATION

### Corresponding Author

*J.-K. Kim. E-mail: mejkkim@ust.hk. Tel: +852 2358 7207. Fax: +852 2358 1543.

### Notes

The authors declare no competing financial interest.

## ACKNOWLEDGMENTS

This project was financially supported by the Research Grants Council of Hong Kong SAR (GRF Project codes: 613811 and 613612). The authors also appreciate the technical assistance from the Materials Characterization and Preparation Facilities (MCPF) and the Department of Chemical and Biomolecular Engineering at HKUST.

## REFERENCES

(1) Ji, L.; Lin, Z.; Alcoutlabi, M.; Zhang, X. Recent Developments in Nanostructured Anode Materials for Rechargeable Lithium-Ion Batteries. *Energy Environ. Sci.* **2011**, *4*, 2682−2699.

(2) Kucinskis, G.; Bajars, G.; Kleperis, J. Graphene in Lithium Ion Battery Cathode Materials: A Review. *J. Power Sources* **2013**, *240*, 66−79.

(3) Brownson, D. A. C.; Kampouris, D. K.; Banks, C. E. An Overview of Graphene in Energy Production and Storage Applications. *J. Power Sources* **2011**, *196*, 4873−4885.

(4) Zhang, B.; Yu, Y.; Huang, Z. D.; He, Y. B.; Jang, D. H.; Yoon, W. S.; Mai, Y. W.; Kang, F. Y.; Kim, J. K. Exceptional Electrochemical Performance of Freestanding Electrospun Carbon Nanofiber Anodes Containing Ultrafine $SnO_x$ Particles. *Energy Environ. Sci.* **2012**, *5*, 9895−9902.

(5) Sun, H.; Sun, X.; Hu, T.; Yu, M.; Lu, F.; Lian, J. Graphene-Wrapped Mesoporous Cobalt Oxide Hollow Spheres Anode for High-Rate and Long-Life Lithium Ion Batteries. *J. Phys. Chem. C* **2014**, *118*, 2263−2272.

(6) Zhu, X.; Zhu, Y.; Murali, S.; Stoller, M. D.; Ruoff, R. S. Nanostructured Reduced Graphene Oxide/$Fe_2O_3$ Composite as a High-Performance Anode Material for Lithium Ion Batteries. *ACS Nano* **2011**, *5*, 3333−3338.

(7) Lai, H.; Li, J.; Chen, Z.; Huang, Z. Carbon Nanohorns as a High-Performance Carrier for $MnO_2$ Anode in Lithium-Ion Batteries. *ACS Appl. Mater. Interfaces* **2012**, *4*, 2325−2328.

(8) Li, W. Y.; Xu, L. N.; Chen, J. $Co_3O_4$ Nanomaterials in Lithium-Ion Batteries and Gas Sensors. *Adv. Funct. Mater.* **2005**, *15*, 851−857.

(9) Sun, Y.; Hu, X.; Luo, W.; Huang, Y. Self-Assembled Mesoporous CoO Nanodisks as a Long-Life Anode Material for Lithium-Ion Batteries. *J. Mater. Chem.* **2012**, *22*, 13826−13831.

(10) Yu, M.; Shao, D.; Lu, F.; Sun, X.; Sun, H.; Hu, T.; Wang, G.; Sawyer, Sh.; Qiu, H.; Lian, J. ZnO/Graphene Nanocomposite Fabricated by High Energy Ball Milling with Greatly Enhanced Lithium Storage Capability. *Electrochem. Commun.* **2013**, *34*, 312−315.

(11) Reddy, M. V.; Rao, G. V. S.; Chowdari, B. V. R. Metal Oxides and Oxysalts as Anode Materials for Li Ion Batteries. *Chem. Rev.* **2013**, *113*, 5364−5457.

(12) Wang, Z.; Zhou, L.; Lou, X. W. Metal Oxide Hollow Nanostructures for Lithium-Ion Batteries. *Adv. Mater.* **2012**, *24*, 1903−1911.

(13) Jiang, J.; Li, Y.; Liu, J.; Huang, X.; Yuan, C.; Lou, X. W. Recent Advances in Metal Oxide-based Electrode Architecture Design for Electrochemical Energy Storage. *Adv. Mater.* **2012**, *24*, 5166−5180.
(14) Zhang, B.; Xu, Z. L.; He, Y. B.; Abouali, S.; Akbari Garakani, M.; Kamali Heidari, E.; Kang, F.; Kim, J. K. Exceptional Rate Performance of Functionalized Carbon Nanofiber Anodes Containing Nanopores Created by (Fe) Sacrificial Catalyst. *Nano Energy* **2014**, *4*, 88−96.
(15) Lin, J.; Peng, Z.; Xiang, C.; Ruan, G.; Yan, Z.; Natelson, D.; Tour, J. M. Graphene Nanoribbon and Nanostructured $SnO_2$ Composite Anodes for Lithium Ion Batteries. *ACS Nano* **2013**, *7*, 6001−6006.
(16) Wu, Z. S.; Zhuo, G.; Yin, L. C.; Ren, W.; Li, F.; Cheng, H. M. Graphene/Metal Oxide Composite Electrode Materials for Energy Storage. *Nano Energy* **2012**, *1*, 107−131.
(17) Sun, Y.; Wu, Q.; Shi, G. Graphene based New Energy Materials. *Energy Environ. Sci.* **2011**, *4*, 1113−1132.
(18) Wang, G.; Shen, X.; Yao, J.; Park, J. Graphene Nanosheets for Enhanced Lithium Storage in Lithium Ion Batteries. *Carbon* **2009**, *47*, 2049−2053.
(19) Chen, D.; Ji, G.; Ma, Y.; Lee, J. Y.; Lu, J. Graphene-Encapsulated Hollow $Fe_3O_4$ Nanoparticle Aggregates as a High-Performance Anode Material for Lithium Ion Batteries. *ACS Appl. Mater. Interfaces* **2011**, *3*, 3078−3083.
(20) Li, C.; Shi, G. Three-Dimensional Graphene Architectures. *Nanoscale* **2012**, *4*, 5549−5563.
(21) Chen, Z.; Ren, W.; Gao, L.; Liu, B.; Pei, S.; Cheng, H. M. Three-Dimensional Flexible and Conductive Interconnected Graphene Networks Grown by Chemical Vapour Deposition. *Nat. Mater.* **2011**, *10*, 424−428.
(22) Xu, Y.; Sheng, K.; Li, C.; Shi, G. Self-Assembled Graphene Hydrogel *via* a One-Step Hydrothermal Process. *ACS Nano* **2010**, *4*, 4324−4330.
(23) Nardecchia, S.; Carriazo, D.; Ferrer, M. L.; Gutiérrez, M. C.; del Monte, F. Three Dimensional Macroporous Architectures and Aerogels Built of Carbon Nanotubes and/or Graphene: Synthesis and Applications. *Chem. Soc. Rev.* **2013**, *42*, 794−830.
(24) Jiang, X.; Yang, X.; Zhu, Y.; Shen, J.; Fan, K.; Li, C. In Situ Assembly of Graphene Sheets-Supported $SnS_2$ Nanoplates into 3D Macroporous Aerogels for High-Performance Lithium Ion Batteries. *J. Power Sources* **2013**, *237*, 178−186.
(25) Chen, W.; Li, S.; Chen, C.; Yan, L. Self-Assembly and Embedding of Nanoparticles by In Situ Reduced Graphene for Preparation of a 3D Graphene/Nanoparticle Aerogel. *Adv. Mater.* **2011**, *23*, 5679−5683.
(26) Yu, Y.; Zhang, B.; He, Y. B.; Huang, Z. D.; Oh, S. W.; Kim, J. K. Mechanisms of Capacity Degradation in Reduced Graphene Oxide/$\alpha$-$MnO_2$ Nanorod Composite Cathodes of Li−Air Batteries. *J. Mater. Chem. A* **2013**, *1*, 1163−1170.
(27) Kamali Heidari, E.; Zhang, B.; Sohi, M. H.; Ataie, A.; Kim, J. K. Sandwich-Structured Graphene-$NiFe_2O_4$-Carbon Nanocomposite Anodes with Exceptional Electrochemical Performance for Li Ion Batteries. *J. Mater. Chem. A* **2014**, *2*, 8314−8322.
(28) Geng, Y.; Wang, S. J.; Kim, J. K. Preparation of Graphite Nanoplatelets and Graphene Sheets. *J. Colloid Interface Sci.* **2009**, *336*, 592−598.
(29) Zheng, Q.; Ip, W. H.; Lin, X.; Yousefi, N.; Yeung, K. K.; Li, Z.; Kim, J. K. Transparent Conductive Films Consisting of Ultralarge Graphene Sheets Produced by Langmuir-Blodgett Assembly. *ACS Nano* **2011**, *5*, 6039−6051.
(30) Pei, S.; Cheng, H. M. The Reduction of Graphene Oxide. *Carbon* **2012**, *50*, 3210−3228.
(31) Wang, X.; Huang, S.; Zhu, L.; Tian, X.; Li, S.; Tang, H. Correlation Between the Adsorption Ability and Reduction Degree of Graphene Oxide and Tuning of Adsorption of Phenolic Compounds. *Carbon* **2014**, *69*, 101−112.
(32) Sharma, Y.; Sharma, N.; Rao, G. V. S.; Chowdari, B. V. R. Nano-$(Cd_{1/3}Co_{1/3}Zn_{1/3})CO_3$: A New and High Capacity Anode Material for Li-Ion Batteries. *J. Mater. Chem.* **2009**, *19*, 5047−5054.
(33) Cabana, J.; Monconduit, L.; Larcher, D.; Palacín, M. R. Beyond Intercalation-based Li-Ion Batteries: The State of the Art and Challenges of Electrode Materials Reacting Through Conversion Reactions. *Adv. Energy Mater.* **2010**, *22*, E170−E192.
(34) Xiong, S.; Chen, J. S.; Lou, X. W.; Zeng, H. C. Mesoporous $Co_3O_4$ and CoO@C Topotactically Transformed from Chrysanthemum-like $Co(CO_3)_{0.5}(OH)\cdot 0.11H_2O$ and Their Lithium-Storage Properties. *Adv. Funct. Mater.* **2012**, *22*, 861−871.
(35) Zhu, J.; Kumar Sharma, Y.; Zeng, Z.; Zhang, X.; Srinivasan, M.; Mhaisalkar, S.; Zhang, H.; Hng, H. H.; Yan, Q. Cobalt Oxide Nanowall Arrays on Reduced Graphene Oxide Sheets with Controlled Phase, Grain Size, and Porosity for Li-Ion Battery Electrodes. *J. Phys. Chem. C* **2011**, *115*, 8400−8406.
(36) Xiao, L.; Wu, D.; Han, S.; Huang, Y.; Li, S.; He, M.; Zhang, F.; Feng, X. Self-Assembled $Fe_2O_3$/Graphene Aerogel with High Lithium Storage Performance. *ACS Appl. Mater. Interfaces* **2013**, *5*, 3764−3769.
(37) Yang, J.; Frost, R. L. Synthesis and Characterisation of Cobalt Hydroxy Carbonate $Co_2CO_3(OH)_2$ Nanomaterials. *Spectrochim. Acta, Part A* **2011**, *78*, 420−428.
(38) Huang, S.; Jin, Y.; Jia, M. Preparation of Graphene/$Co_3O_4$ Composites by Hydrothermal Method and Their Electrochemical Properties. *Electrochim. Acta* **2013**, *95*, 139−145.
(39) Stoch, J.; Kukucz, J. G. The Effect of Carbonate Contaminations on XPS O 1s Band Structure in Metal Oxides. *Surf. Interface Anal.* **1991**, *17*, 165−167.
(40) Yang, J.; Liu, H.; Martens, W. N.; Frost, R. L. Synthesis and Characterization of Cobalt Hydroxide, Cobalt Oxyhydroxide, and Cobalt Oxide Nanodiscs. *J. Phys. Chem. C* **2010**, *114*, 111−119.
(41) Porta, P.; Dragone, R.; Fierro, G.; Inversi, M.; Jacono, M. L.; Moretti, G. Preparation and Characterization of Cobalt-Copper Hydroxysalts and Their Oxide Products of Decomposition. *J. Chem. Soc., Faraday Trans.* **1992**, *88*, 311−319.
(42) Varghese, B.; Hoong, T. C.; Yanwu, Z.; Reddy, M. V.; Chowdari, B. V. R.; Wee, A. T. S.; Vincent, T. B. C.; Lim, C. T.; Sow, C. H. $Co_3O_4$ Nanostructures with Different Morphologies and Their Field-Emission Properties. *Adv. Funct. Mater.* **2007**, *17*, 1932−1939.
(43) Xiong, S.; Yuan, C.; Zhang, X.; Xi, B.; Qian, Y. Controllable Synthesis of Mesoporous $Co_3O_4$ Nanostructures with Tunable Morphology for Application in Supercapacitors. *Chem.—Eur. J.* **2009**, *15*, 5320−5326.
(44) Petitto, S. C.; Marsh, E. M.; Carson, G. A.; Langell, M. Cobalt Oxide Surface Chemistry: The Interaction of CoO (100), $Co_3O_4$ (110), and $Co_3O_4$ (111) with Oxygen and Water. *J. Mol. Catal. A: Chem.* **2008**, *281*, 49−58.
(45) Aragón, M. J.; León, B.; Vicente, C. P.; Tirado, J. L. A New Form of Manganese Carbonate for the Negative Electrode of Lithium-Ion Batteries. *J. Power Sources* **2011**, *196*, 2863−2866.
(46) Shao, L.; Ma, R.; Wu, K.; Shui, M.; Lao, M.; Wang, D.; Long, N.; Ren, Y.; Shu, J. Metal Carbonates as Anode Materials for Lithium Ion Batteries. *J. Alloys Compd.* **2013**, *581*, 602−609.
(47) Su, L.; Zhou, Z.; Qin, X.; Tang, Q.; Wu, D.; Shen, P. $CoCO_3$ Submicrocube/Graphene Composites with High Lithium Storage Capability. *Nano Energy* **2013**, *2*, 276−282.
(48) Ding, Z.; Yao, B.; Feng, J.; Zhang, J. Enhanced Rate Performance and Cycling Stability of a $CoCO_3$-Polypyrrole Composite for Lithium Ion Battery Anodes. *J. Mater. Chem. A* **2013**, *1*, 11200−11209.
(49) Choi, B. G.; Chang, S. J.; Lee, Y. B.; Bae, J. S.; Kim, H. J.; Huh, Y. S. 3D Heterostructured Architectures of $Co_3O_4$ Nanoparticles Deposited on Porous Graphene Surface for High Performance of Lithium Ion Batteries. *Nanoscale* **2012**, *4*, 5924−5930.
(50) Huang, X. H.; Tu, J. P.; Zhang, B.; Zhang, C. Q.; Li, Y.; Yuan, Y. F.; Wu, H. M. Electrochemical Properties of NiO−Ni Nanocomposite as Anode Material for Lithium Ion Batteries. *J. Power Sources* **2006**, *161*, 541−544.
(51) Wu, Z. S.; Ren, W.; Wen, L.; Gao, L.; Zhao, J.; Chen, Z.; Zhou, G.; Li, F.; Cheng, H. M. Graphene Anchored with $Co_3O_4$ Nanoparticles as Anode of Lithium Ion Batteries with Enhanced

Reversible Capacity and Cyclic Performance. *ACS Nano* **2010**, *4*, 3187−3194.
(52) Yang, X.; Fan, K.; Zhu, Y.; Shen, J.; Jiang, X.; Zhao, P.; Luan, S.; Li, C. Electric Papers of Graphene-Coated $Co_3O_4$ Fibers for High-Performance Lithium-Ion Batteries. *ACS Appl. Mater. Interfaces* **2013**, *5*, 997−1002.
(53) Kim, H.; Seo, D. H.; Kim, S. W.; Kim, J.; Kang, K. Highly Reversible $Co_3O_4$/Graphene Hybrid Anode for Lithium Rechargeable Batteries. *Carbon* **2011**, *49*, 326−332.
(54) Qiu, D.; Bu, G.; Zhao, B.; Lin, Z.; Pu, L.; Pan, L.; Shi, Y. In Situ Growth of Mesoporous $Co_3O_4$ Nanoparticles on Graphene as a High-Performance Anode Material for Lithium-Ion Batteries. *Mater. Lett.* **2014**, *119*, 12−15.
(55) Hao, F.; Zhang, Z.; Yin, L. $Co_3O_4$/Carbon Aerogel Hybrids as Anode Materials for Lithium Ion Batteries with Enhanced Electrochemical Properties. *ACS Appl. Mater. Interfaces* **2013**, *5*, 8337−8344.
(56) Chen, S. Q.; Wang, Y. Microwave-Assisted Synthesis of a $Co_3O_4$−Graphene Sheet-on-Sheet Nanocomposite as a Superior Anode Material for Li-ion Batteries. *J. Mater. Chem.* **2010**, *20*, 9735−9739.